FIA 2020/22
XII CONGRESSO/CONGRESO IBEROAMERICANO DE ACÚSTICA
XXIX ENCONTRO DA SOCIEDADE BRASILEIRA DE ACÚSTICA - SOBRAC
Florianópolis, SC, Brasil

Wave-number analysis of the measurement of finite absorbers with a microphone array

Brandão, E.[1]**; Fernandez-Grande, E.**[2]

[1] Acoustical Engineering & Civil Engineering Graduate Program, Federal University of Santa Maria (UFSM), Santa Maria-RS, 97050-140, Brazil, eric.brandao@eac.ufsm.br

[2] Department of Electrical Engineering, Technical University of Denmark (DTU), Ørsteds Plads, Building 352, 2800, Kgs. Lyngby, Denmark, efg@elektro.dtu.dk

Abstract

This paper aims at analyzing the effect of edge diffraction on the in situ impedance measurement with an array of microphones. An analytical solution for the problem is presented, based on a two-dimensional Fourier transform of the sound field above a rectangular sample. A simplified Boundary Element Method (BEM) is used to emulate the measurement of finite samples with a microphone array, and the wave-number spectrum is estimated by a regularized solution of the inverse problem. The properties of the observed wave-number spectrum are associated either with the specular reflection or with the diffracted components, caused by the interaction of the sound wave with the finite absorber. The absorption coefficient is retrieved from the regularized solution and the influence of the size and shape of the samples is also investigated.

Keywords: impedance measurement; diffraction; microphone array; wave-number domain.

PACS: 43.55.Ev; 43.60.Pt; 43.20.Fn.

1. INTRODUCTION

The absorption coefficient is an important property in many noise and reverberation control applications. Under normal incidence, ISO 10534-2 [1] regulates the measurement procedures, valid only for a plane wave at an elevation angle of 0°. Under diffuse incidence, the standard ISO 354 [2] regulates the measurement of an averaged absorption coefficient across all angles of incidence. In each noise or reverberation control application, the applied sample may vary in size and shape, and so will vary the diffraction created by the sample. On the other hand, for any given measurement method, it can be advantageous to characterize the impedance/absorption properties with minimal influence of the size and shape of the sample under test.

One of the main concerns when measuring the absorption coefficient *in situ* or under diffuse field conditions is the analysis of the influence of the finite dimensions of the sample. At the interface between the sample and its surroundings, the abrupt change in the boundary conditions will cause the sound wave to diffract, which is known as the edge diffraction effect. It is well known that it plays an important role in measurements of sound absorption under diffuse incidence, for which it can exceed unity [3–5].

Concerning the free-field or *in situ* measurement conditions, there are several methods that can be used [6], and the edge diffraction effect has always been of interest in such context. Kimura and Yamamoto [7] investigated tried to determine the minimum required size of a specimen for the accurate measurement of the absorption coefficient under oblique incidence. In Refs. [8, 9], the edge diffraction effect was investigated numerically and experimentally. The Boundary Element Method (BEM) was used to demonstrate the effect of the finiteness of porous absorbers measured under free-field conditions. Both works used single point measurement techniques (i.e. a pressure-particle velocity probe) and identified that the edge diffraction causes the resulting absorption coefficient to oscillate around the true absorption of an infinite sample. Thus, such measurement techniques are sample size dependent.

The use of microphone arrays to measure the sound absorption *in situ* has gained some attention in recent years, following past work of Tamura [10, 11]. This is an ill-posed inverse problem and many types of arrays can be used such as spherical, double-layered, and randomized arrays [12–14]. The sound field model has been formulated using different bases such as propagating plane waves [12, 13], propagating and evanescent plane waves [15, 16], and by distributed monopoles with sparse processing [14]. The absorption coefficient can be estimated either by reconstructing the surface impedance [12, 14, 15] or by using the acoustic power of the estimated wave-number spectrum [13]. Investigations of the finite size effect on the estimated absorption coefficient was exploited in Refs. [15–17].

This study is a follow-up to a recent paper published in the Journal of the Acoustical Society of America [18] to analyze the edge diffraction effect near finite porous absorbers in the wave-number domain. Sections 2 and 3 re-introduce the theoretical analysis of the wave-number spectrum and the inverse problem used to estimate it from data of an array of pressure sensors. The Boundary Element Model used to simulate the sound field above finite is summarized in Sec. 4. The main differences of this paper w.r.t. Ref. [18] is the analysis of samples with different flow resistivity and the inclusion of the wave-number spectrum of circular samples. The results and discussion for these scenarios are provided in Sec. 5, followed by conclusions in Sec. 6.

2. THEORETICAL ANALYSIS OF THE WAVE-NUMBER SPECTRUM

The derivation of the analytical solution for the wave-number spectrum is based on the problem studied by Refs. [3, 16, 19]. The total acoustic field above a finite absorber will consist of one plane incident wave, one plane geometrically reflected wave and the scattered field, as in the following equation

$$p(\mathbf{r}) = \tilde{p}_i \mathrm{e}^{-\mathrm{j}\mathbf{k}_i \cdot \mathbf{r}} + \tilde{p}_i \mathrm{e}^{-\mathrm{j}\mathbf{k}_r \cdot \mathbf{r}} - \frac{2\mathrm{j}\,\tilde{p}_i k}{Z_s(\theta) + Z_r(\theta,\phi)} \times \int_S G(\mathbf{r},\mathbf{r}_s)\, \mathrm{e}^{-\mathrm{j}\,(k_x' x_s + k_y' y_s)}\, \mathrm{d}S\,, \tag{1}$$

where $\mathbf{r} = (x_\mathrm{r}, y_\mathrm{r}, z_\mathrm{r})$ is the coordinate vector of a receiver and $\mathbf{r}_\mathrm{s}$ is a coordinate vector on the surface of the finite absorber (see Fig. 1 for reference), S is the surface area of the absorber, $k = \omega/c$ is the wave-number of the air, and $\tilde{p}_i$ is the complex amplitude of the incident plane wave. $G(\mathbf{r},\mathbf{r}_s) = \frac{\mathrm{e}^{-\mathrm{j}kr}}{2\pi r}$ is the half space Green's function, with $r = \sqrt{(x_\mathrm{r}-x_\mathrm{s})^2 + (y_\mathrm{r}-y_\mathrm{s})^2 + z_\mathrm{r}^2}$. θ and ϕ are the elevation and azimuth angle of incidence of the impinging plane wave. $\mathbf{k}_i = (k_x', k_y', -k_z')$ and $\mathbf{k}_r = (k_x', k_y', k_z')$ are the wave-numbers of the incident and reflected plane waves, with $k_x' = k\sin(\theta)\cos(\phi)$, $k_y' = k\sin(\theta)\sin(\phi)$, and $k_z' = k\cos(\theta)$ [5]. $Z_s(\theta)$ is the normalized surface impedance of the sample, and $Z_r(\theta,\phi)$ is the normalized radiation impedance of the finite absorber. For a rectangular sample, the radiation impedance is given in Ref. [19] and can be integrated numerically [5, 16]. Note that Eq. (1)is valid for non-locally reacting samples.

The derivation of the wave-number spectrum is acomplished by taking the 2D spatial Fourier transform of Eq. (1) at an infinite plane z_r above the sample. The steps are detailed in Ref. [18], and only rectangular samples are accounted for in this analytical derivation. For the first term on the right-hand side of Eq. (1), the incident wave-number spectrum is $P_i(k_x,k_y) = \tilde{p}_i 4\pi^2 \mathrm{e}^{-\mathrm{j}k_z' z_\mathrm{r}}\,\delta(k_x - k_x', k_y - k_y')$, an impulse associated with the direction of travel of the incoming plane wave. Similarly, for the second and third terms on the right-hand side of Eq. (1), the reflected wave-number spectrum is

$$P_r(k_x,k_y) = \tilde{p}_i 4\pi^2 \mathrm{e}^{\mathrm{j}k_z' z_\mathrm{r}}\,\delta(k_x - k_x', k_y - k_y') + \frac{2k\tilde{p}_i\, L_x L_y}{Z_s(\theta) + Z_r(\theta,\phi)} \frac{\mathrm{e}^{-\mathrm{j}k_z z_\mathrm{r}}}{k_z} S(k_x,k_y)\,, \tag{2}$$

$$S(k_x,k_y) = \mathrm{sinc}\left[\frac{(k_x - k_x')L_x}{2}\right] \mathrm{sinc}\left[\frac{(k_y - k_y')L_y}{2}\right], \tag{3}$$

with $k_z' = (k^2 - k_x'^2 - k_y'^2)^{1/2}$ and $k_z = (k^2 - k_x^2 - k_y^2)^{1/2}$.

This result provides insight into the edge diffraction phenomenon. As with the incident field, the first term on the right-hand side of Eq. (2) represents an impulse associated with the direction of travel of the specular reflection. In the case of an infinite absorber, this would be the only component in the wave-number spectrum (scaled by the reflection coefficient). The second term shows the influence of the finiteness of the absorber through a two-dimensional sinc function, scaled by $Z_s(\theta)$ and $Z_r(\theta,\phi)$. The main lobe of this function is associated with a plane wave traveling in the direction of the specular reflection. The other lobes result from the effects of the finiteness of the absorber. The lobes can be either associated with propagating or evanescent plane waves, traveling in directions other than the direction of the specular reflection. Particularly, the lobes associated with evanescent waves are associated with plane wave components traveling in directions parallel to the surface of the sample. The magnitudes of the side lobes tend to decay as the spatial frequency increases. Such effects will be further discussed in Sec. 5.

3. WAVE-NUMBER SPECTRUM ESTIMATION FROM ARRAY DATA

The wave-number spectrum is estimated from data collected by an array of sensors, by solving the inverse problem. Herein, the estimation is based on the Near-Field Acoustical Holography (NAH) [20]. Consider a set of $\mathfrak{M}$ receiver points, representing an array with each receiver at coordinate $\mathbf{r}_\mathrm{m}$. The measured data at the microphone positions can be projected into a basis of $\mathfrak{L}$ propagating and evanescent plane waves. A matrix equation representing this problem is given by

$$\tilde{\mathbf{p}} = \mathbf{H}\,\mathbf{x} + \mathbf{n}\,, \tag{4}$$

where $\tilde{\mathbf{p}} \in \mathbb{C}^{\mathfrak{M}}$ represents the sound pressure captured by the $\mathfrak{M}$ microphones at a given frequency. $\mathbf{x} \in \mathbb{C}^{\mathfrak{L}}$ are the unknown complex amplitudes of the $\mathfrak{L}$ plane waves and $\mathbf{n}$ represents the effects of noise and model inconsistencies [13, 14, 21]. Each $\ell - th$ plane wave has wave-number $\mathbf{k}_\ell = (k_x, k_y, k_z)$, with k_z given by

$$k_z = \begin{cases} \sqrt{k^2 - (k_x^2 + k_y^2)}, & \text{if } k_x^2 + k_y^2 \leq k^2 \\ -\mathrm{j}\sqrt{(k_x^2 + k_y^2) - k^2}, & \text{if } k_x^2 + k_y^2 > k^2 \end{cases}, \tag{5}$$

where the components with $k_x^2 + k_y^2 \leq k^2$ represent propagating plane waves, radiated to the far-field, and the components with $k_x^2 + k_y^2 > k^2$ represent evanescent plane waves, with power flowing parallel to the (x,y) plane, but decaying exponentially in the $\hat{z}$ direction [20]. In order to capture information of the incident and reflected/scattered sound fields, $\mathbf{H} = [\mathbf{H}_\mathrm{inc} \;\; \mathbf{H}_\mathrm{ref}] \in \mathbb{C}^{\mathfrak{M}\times\mathfrak{L}}$ is the sensing matrix composed of a dictionary of incident, $\mathbf{H}_\mathrm{inc}$, and reflected, $\mathbf{H}_\mathrm{ref}$, plane waves. For a given receiver at $\mathbf{r}_\mathrm{m} = (x,y,z)$ and a wave-number $\mathbf{k}_\ell$, the matrices' elements are

$$\begin{aligned} \psi_\ell^{\mathrm{inc}}(\mathbf{r}_\mathrm{m}) &= \mathrm{e}^{-\mathrm{j}\,(k_x x + k_y y + k_z (z - z^+))} \\ \psi_\ell^{\mathrm{ref}}(\mathbf{r}_\mathrm{m}) &= \mathrm{e}^{-\mathrm{j}\,(k_x x + k_y y - k_z (z - z^-))} \end{aligned}\,, \tag{6}$$

with z^+ and z^- being the locations of the incident and reflected virtual source planes, which serves as a balance between regularizing the inverse problem and including the information of the evanescent waves [21, 22].

Usually $\mathfrak{L} \gg \mathfrak{M}$ and Eq. (4) becomes an underdetermined ill-posed inverse problem. Herein, it is solved with Tikhonov regularization [12, 23], which is expressed by

$$\tilde{\mathbf{x}} = \underset{\mathrm{x}}{\mathrm{argmin}} \left(\|\mathbf{H}\mathbf{x} - \tilde{\mathbf{p}}\|_2^2 + \lambda^2 \|\mathbf{x}\|_2^2 \right)\,, \tag{7}$$

where $\tilde{x}$ is the estimation of the complex amplitudes of the $\mathfrak{L}$ plane waves and $\lambda > 0$ is the regularization parameter, which is estimated herein by the L-curve criterion [24]. Once $\tilde{\mathbf{x}}$ is estimated, one has a representation of the wave-number spectrum to analyze the direction of travel of the incident and the scattered components due to specular reflection and edge diffraction. Furthermore, one can reconstruct the sound field elsewhere in the vicinity of the absorbing sample. The reconstructed sound pressure and particle velocity is expressed in matrix form as $\tilde{\mathbf{p}}_\mathrm{re} = \mathbf{H}_\mathrm{re}\,\tilde{\mathbf{x}}$ and $\tilde{\mathbf{u}}_\mathrm{re} = \frac{-1}{\mathrm{j}k\rho c}\,\nabla\mathbf{H}_\mathrm{re}\,\tilde{\mathbf{x}}$, respectively [23]. Note that

$\tilde{\mathbf{p}}_{\mathrm{re}}$ and $\tilde{\mathbf{u}}_{\mathrm{re}}$ are reconstructed at a set of K positions, and that $\mathbf{H}_{\mathrm{re}} \in \mathbb{C}^{K\times\mathfrak{L}}$ is the reconstruction matrix containing the plane wave functions evaluated at the reconstruction points.

For *in situ* measurements it is interesting to reconstruct the sound pressure and the normal component of the particle velocity at a set of points at the surface of the sample. Thus, the reconstructed surface impedance and the absorption coefficient can be estimated as

$$\tilde{Z}_s(\mathbf{r}_s) = -\frac{1}{\rho c}\frac{\tilde{p}(\mathbf{r}_s)}{\tilde{u}_n(\mathbf{r}_s)}\,, \tag{8}$$

$$\alpha = 1 - \left|\frac{\bar{Z}_s\cos(\theta)-1}{\bar{Z}_s\cos(\theta)+1}\right|^2\,, \tag{9}$$

where θ is the incidence angle and $\bar{Z}_s$ is the spatial average of several reconstructed surface impedances on a grid of K points. This is done to alleviate the effect of errors present in the reconstruction process [14] and to obtain a single value for Z_s. Typically, the grid is small enough to ensure not too large spatial variations of Z_s in the frequency range of interest [14].

4. SIMULATION FRAMEWORK

Numerical simulations are performed to analyze the sound field caused by a monopole above finite samples located at the plane $z=0$. To keep the analysis constrained to the edge diffraction effect, we consider only locally-reacting samples. For the following, the scheme in Fig. 1a depicts a monopole source at $\mathbf{r}_{\mathrm{q}} = (x_{\mathrm{q}}, y_{\mathrm{q}}, z_{\mathrm{q}})$, the mirrored monopole at $\mathbf{r}_{\mathrm{q}} = (x_{\mathrm{q}}, y_{\mathrm{q}}, -z_{\mathrm{q}})$, and a receiver at $\mathbf{r} = (x_{\mathrm{r}}, y_{\mathrm{r}}, z_{\mathrm{r}})$. Spherical waves traveling from the source to sample/baffle structure will suffer diffraction shown schematically in the figure.

For a finite and locally-reacting sample, flush-mounted on an infinite hard baffle at $z=0$, the sound field can be calculated by the Helmholtz/Huygens integral equation [8, 9]. A simplified Boundary Element Method (BEM) is used to compute the sound pressure at the surface of the sample (stage 1) and the sound pressure at a given receiver at $\mathbf{r}$ (stage 2). To do so, the surface of the sample is discretized in a mesh of N triangular elements, with at least 6 elements

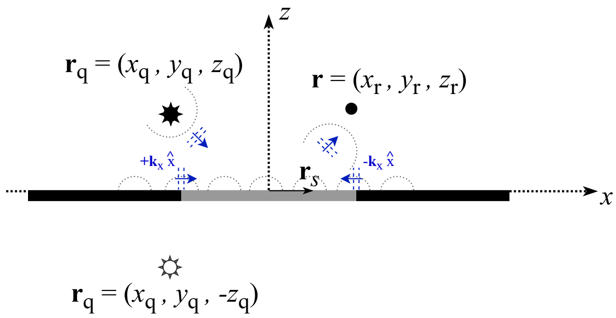

(a) Schematics

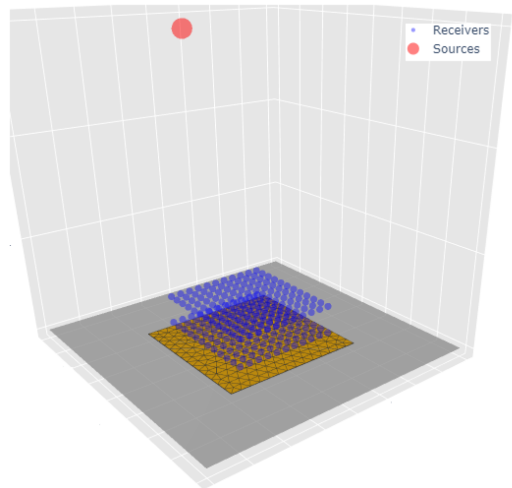

(b) BEM scene

Figura 1: Sound field simulation schematics and BEM scene. The sample is finite and embedded on a infinite hard baffle. (a) - The circular dotted lines represent spherical waves emanating from the sound source and due to diffraction at sample/baffle structure. The arrows and dashed lines in blue represent the incident and specular reflected propagating plane waves and the evanescent components traveling parallel to the x-axis. (b) - The mesh of the sample is represented in yellow, the blue dots represent the array of microphones, and the red dot represents the sound source.

per wavelength for 2000 Hz. The sound pressure at each element in the mesh is assumed to be constant across the surface of the element. The discretized integral equation is given by

$$\vartheta(\mathbf{r})p(\mathbf{r}) = A\left[\frac{\mathrm{e}^{-\mathrm{j}k|\mathbf{r}_1|}}{|\mathbf{r}_1|} + \frac{\mathrm{e}^{-\mathrm{j}k|\mathbf{r}_2|}}{|\mathbf{r}_2|} - \frac{\mathrm{j}k}{\tilde{Z}_s} \times \sum_{n=1}^{N} p(\mathbf{r}_{sn})\int_{S_n}\frac{\mathrm{e}^{-\mathrm{j}k|\mathbf{r}-\mathbf{r}_s|}}{4\pi|\mathbf{r}-\mathbf{r}_s|}\,\mathrm{d}S_n\right]\,, \tag{10}$$

with A is the source strength of 1 kg/s^2, assumed for all further analyses, and $\mathbf{r}_s$ being the integration variable for each element of the absorber; $\vartheta(\mathbf{r})$ is 0.5 for $\mathbf{r}$ located on the absorptive surface and 1.0 for $\mathbf{r}$ at $z > 0$. The surface impedance prescribed to the model varies with frequency, but is the same for all the elements in the mesh. The collocation method and Gaussian quadrature are used to compute the complex amplitude of the sound pressure at the n-th element, $p(\mathbf{r}_{sn})$, as in Ref. [9], and then, one can compute the sound pressure at any receiver point at $z > 0$.

5. RESULTS AND DISCUSSION

In this study, the tested scenarios consist of finite squared samples with dimensions $L \times L$ m^2 or circular samples with radius a [m]. Miki's model [25] is used to compute the characteristic impedance and complex sound speed of a material with flow resistivity of $\sigma = 20000$ Nsm^{-4}. We assume a locally-reacting and hard-backed porous layer of thickness d, for which the surface impedance can be calculated from a well-known Transfer Matrix Method (TMM) [26]. This surface impedance is prescribed as a boundary condition to the model in Sec. 4. Samples with $d = 25$ mm and $d = 100$ mm emulate a low and high absorbent samples, respectively. In all cases investigated, the sound source is at a distance of 1.5 m from the center of the sample. The incidence angle, θ (elevation), is varied and the azimuth angle is $\phi = 0°$. The coordinates of the sound source are such that $x_{\mathrm{q}} \geq 0$, $y_{\mathrm{q}} = 0$ and $z_{\mathrm{q}} > 0$, so that the main incident waves travel in the $-|k_x|$ direction.

The microphones are arranged in a double layer planar array with 0.57×0.65 m^2 and 11×12 sensors in each layer (Fig. 1b). The separation between the layers is 2.9 cm and the distance between the surface of the sample and the closest layer is 1.3 cm. The use of a regularized inversion and the automatic calculation of λ by the L-curve criterion makes it possible to have reliable estimates of the wave-number spectrum, circumventing wrap-around errors associated with discrete Fourier transformations [21, 22].

Gaussian noise was added to all the simulations with a signal-to-noise ratio (SNR) of 35 dB. Regarding the estimation of the wave-number spectrum, the wave components are the propagating waves grid, equiangular over half a sphere and the evanescent components as a regular grid spanning k_x from $-\pi/\Delta_x$ to $+\pi/\Delta_x$ and k_y from $-\pi/\Delta_y$ to $+\pi/\Delta_y$ (outside the radiation circle), with Δ_x and Δ_y being the separation between the microphones in the array in $\hat{x}$ and $\hat{y}$ directions, respectively. Then, Eq. (5) is used to compute k_z and Eq. (6) is used to construct the matrix $\mathbf{H}$. The virtual source planes are located at $z^- = -1.5\Delta$ m and $z^+ = 0.013 + 0.029 + 1.5\Delta$ m, with $\Delta = \max(\Delta_x, \Delta_y)$, as suggested in Refs. [21, 22].

5.1 Wave-number spectra

The figures in this section show the color maps of the normalized magnitude of the wave-number spectrum (k-space). The normalization is done relative to the maximum value of the magnitude in each map. The color maps are plotted as a function of the trace wave-numbers k_x and k_y (the directions of travel of the wave components [23]). Thus, a negative value of k_x is associated with a plane wave traveling on the $-\hat{x}$ direction (see the schematics in Fig. 1a). The radiation circle is plotted as a grey line in each figure, and allows the distinction between propagating ($[k_x^2 + k_y^2]^{1/2} \leq k$) and evanescent plane waves ($[k_x^2 + k_y^2]^{1/2} > k$). All samples analyzed in this section had a thickness of 25 mm.

5.1.1 Theoretical wave-number spectra

First, one can analyze the theoretical and noiseless wave-number spectrum according to the results of Sec. 2 (rectangular samples). To render a plot of Eq. (2), some considerations have to be made. The last term on the right-hand side of the equation will be analyzed. The reason is that for an infinite aperture, the first term, $\delta(k_x - k_x^{'}, k_y - k_y^{'})$, is dominant. In practice, however, a finite aperture will be used, and the impulse term will become a two-dimensional sinc function (instead of a Dirac delta) due to the convolution with the finite aperture's response in the wave-number domain. The last of Eq. (2) has a singularity for $k_z \to 0$ (exactly at the radiation circle), related to the zero normal velocity of grazing waves. To reduce the influence of this physical singularity, the wave-number spectrum was smoothed as described in Refs. [27, 28].

Fig. 2 displays the magnitude of the last term of Eq. (2) for squared samples of $L = 40,\ 60$ and 80 cm and for $\theta = 0°$, $30°$ and $45°$ at the plane $z_r = 0.013$ m. As discussed in Sec. 2, the main lobe of the two-dimensional sinc function is associated with a plane wave traveling in the direction of the specular reflection. The other lobes result from the effects of the finiteness of the absorber and can be either associated with propagating or evanescent plane waves. Their magnitude tends to decrease as the spatial frequency increases, which is an effect of the two-dimensional sinc function and due to the k_z in the denominator of Eq. (2). As the angle of incidence changes, the two-dimensional sinc function is shifted in k-space. In other words, the specular reflection associated with the main lobe shifts its location and so do the side lobes. On a continuous k-space, the width of the main lobe is larger for smaller samples. For higher angles of incidence, part of the main lobe is inside the radiation circle and part is outside. The evanescent components are more prominent for the samples with $L = 40$ cm and $L = 60$ cm and tend to decrease in magnitude as the sample size and/or k_x and k_y increase. As discussed earlier, the evanescent components are associated with waves with a direction of propagation parallel to the (x, y) plane. The locations of the side lobes in the color maps are given by the two-dimensional sinc function in Eq. (2).

5.1.2 Estimated wave-number spectra

In practice, the wave-number spectrum is estimated from data collected by an array of microphones via regularized inversion (Sec. 3). The case of infinite absorbers is studied in Ref. [18]. It is noteworthy that there are no significant side-lobe components on the reflected k-space in such cases. For the wave-number spectra of finite absorbers, the incident k-spaces are very similar for all investigated samples, containing the main lobe associated with the prescribed direction of incidence and side lobes of low magnitude. These results are omitted here for the sake of brevity. From now on, we investigate the reflected part of the wave-number spectrum for rectangular and circular finite samples, and most of the significant side-lobe components can be associated with the diffraction at the edges of the finite absorbers.

Fig. 3 displays the magnitude of the reflected wave-number spectra for squared samples of $L = 40,\ 60$ and 80 cm and for $\theta = 0°$, $30°$ and $45°$. In all cases, it can be noticed that the specular component is the strongest and lies inside the radiation circle. There are several side-lobe wave components, which tend to decrease in magnitude as the sample size and/or k_x and k_y increase. As opposed to the wave-number spectra of the infinite samples [18], these side lobes have significant magnitude and can be attributed to the diffraction of the sound waves on the finite absorber. In comparison to Fig. 2, the specular and side-lobe components are shifted in k-space, as predicted by the theoretical results. Also, the locations of the specular and most of the side-lobe components match what is predicted by Eq. (2). There are also differences to be accounted for. For instance, for the sample with $L = 40$ cm at $\theta = 45°$, the main specular lobe of the theoretical prediction is wide and spans through the inside and outside of the radiation circle. For the regularized solution, the specular lobe is narrower and the side-lobe components are more noticeable (w.r.t. the theoretical wave-number spectra). These differences can be attributed to the discretization of the wave-number spectrum in the regularized solution and to the fact that in the simulated sound field, the incident wavefront is spherical, which renders a more complex sound field in k-space.

The connection between the side-lobe components with significant amplitude with the diffraction effects on finite porous absorbers in the spatial domain can be analyzed. First, let us consider the normal incidence case (left column of Fig. 3), for which the sound source is at $\mathbf{r}_q = (0.0, 0.0, 1.5)$. In such cases, the main reflected plane wave component lies in the center of the color maps. Some of the significant side-lobe components are evanescent plane waves located mainly at $(-k_x, 0)$ or at $(+k_x, 0)$. The former indicates a plane wave traveling from $+x$ to $-x$, linked with diffraction occurring due to the discontinuity of admittances between the sample and the baffle. The latter is associated with wave components traveling in the opposite direction and the same rationale can be applied to the $(0, \pm k_y)$ components. Also note that the evanescent components are symmetric with respect to $k_x = 0$ or

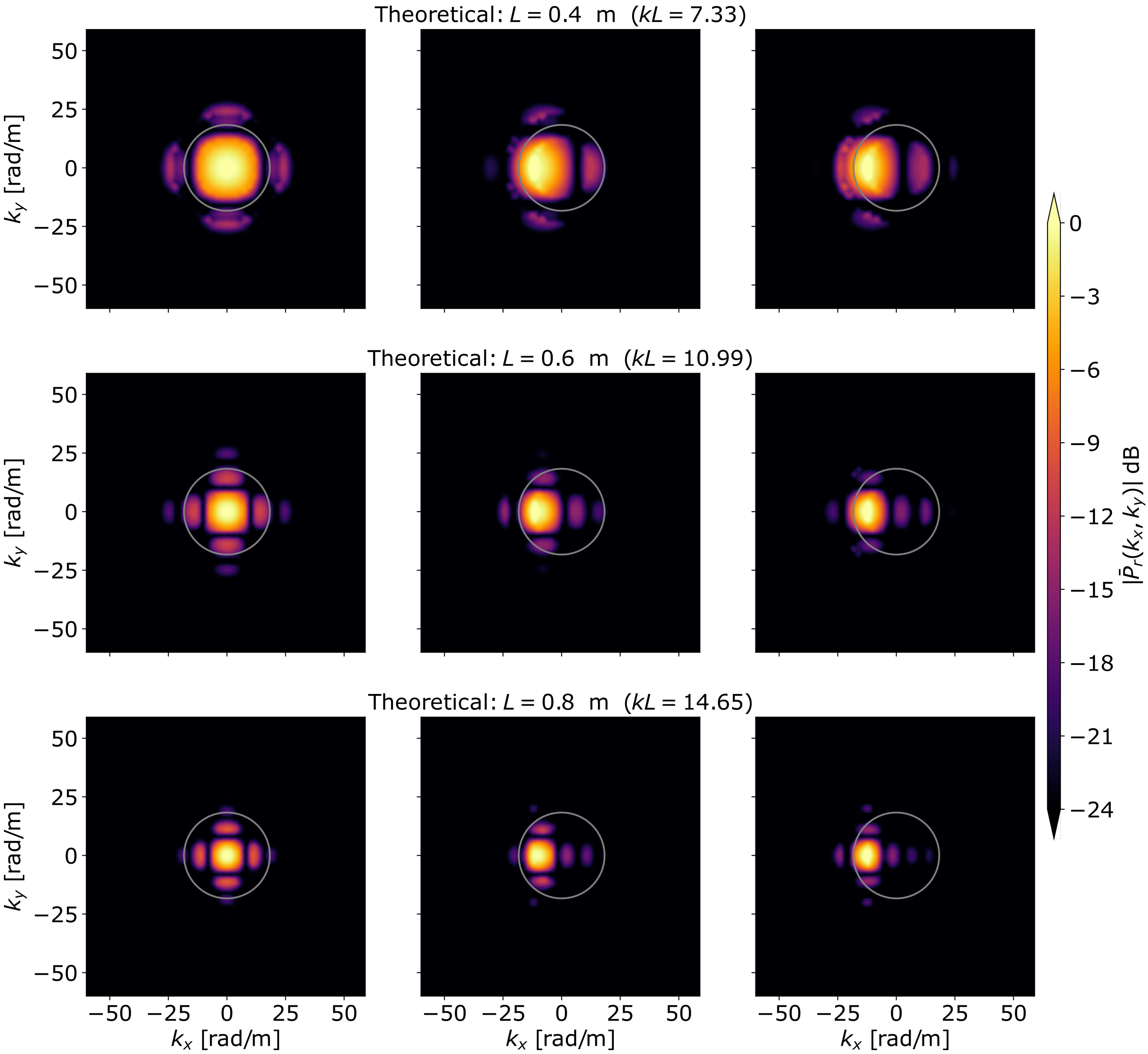

Figura 2: Theoretical wave-number spectra of the last term on right-hand side of Eq. (2). Evaluation at 1 kHz for samples with $L = 40$, 60 and 80 cm (rows) and incidence angles: $\theta = 0°$, $30°$ and $45°$(columns).

$k_y = 0$, as $\theta = 0°$ and $x_q = y_q = 0$ m. The array used has a slightly smaller dimension in the $\hat{x}$ direction, which creates the differences on the k-space for the k_x and k_y axis.

Let us consider the oblique incidence cases. The center column of Fig. 3 shows the k-space magnitude for an incidence angle of $\theta = 30°$, with the sound source at $\mathbf{r}_q = (0.75, 0.00, 1.30)$. Thus, the main reflected plane wave component is $\mathbf{k}_r = (-9.16, 0.00, 15.86)$. The propagating and evanescent components are shifted towards $-|k_x|$, as predicted by the theoretical k-space in Fig. 2. For the $L = 60$ cm sample, there is one evanescent component at $\approx (-25, 0)$ rad/m, associated with waves traveling from $+x$ to $-x$, and two other evanescent components at $\approx (-8, \pm 25)$ rad/m associated to waves traveling in a direction somewhat shifted towards the diagonal of the sample. As the sound source is closer to the edge at $+L/2$, the sound field is stronger at locations near this edge, originating such diffracted wave components. The same rationale applies to the right most column of Fig. 3, valid for $\theta = 45°$.

Now, we consider a circular sample of radius $a = 20$ cm. Fig. 4 displays the magnitude of the reflected wave-number spectra for $\theta = 0°$, $30°$ and

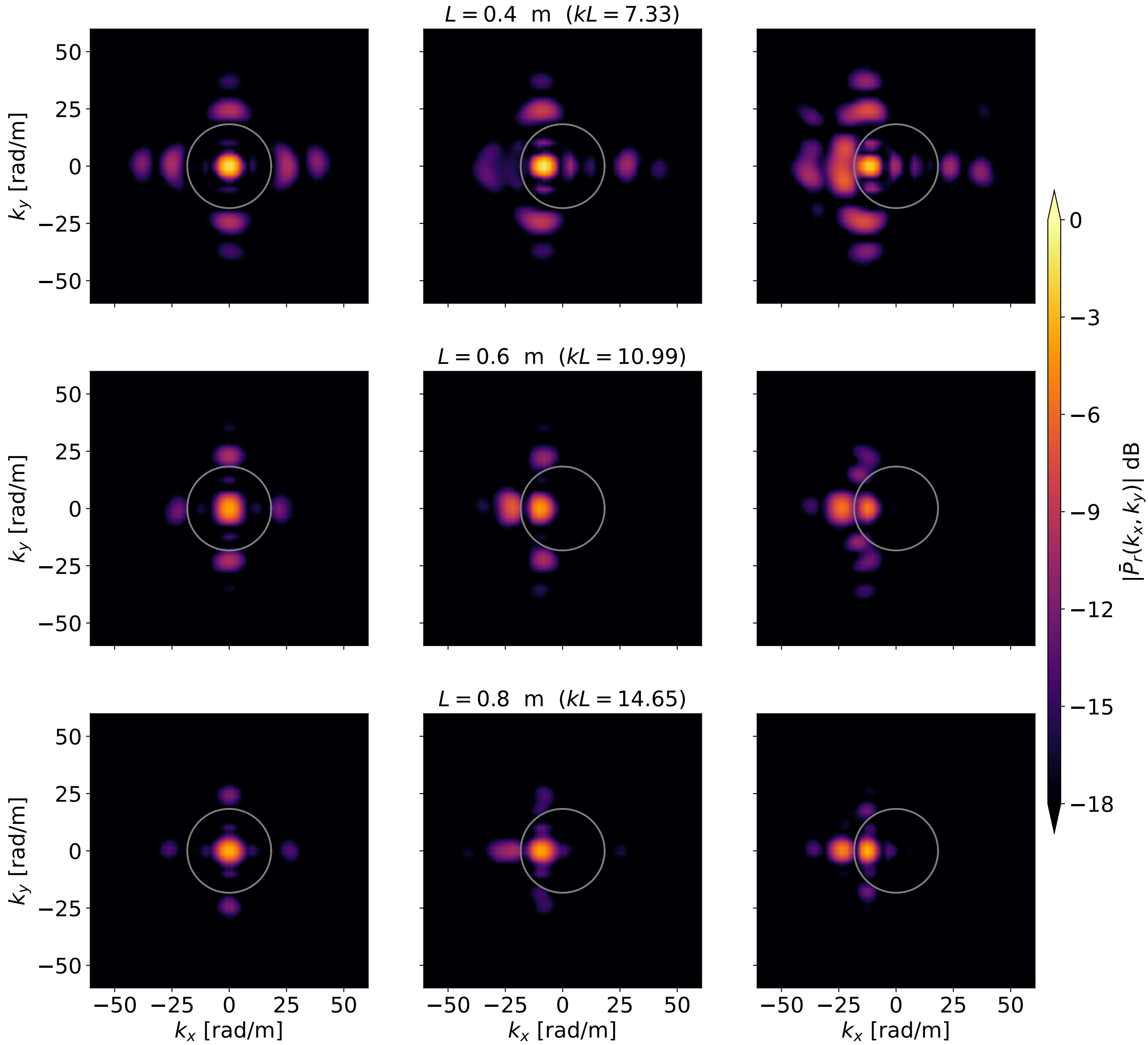

Figura 3: Reflected wave-number spectra at 1000 Hz for samples of sizes: $L = 40,\ 60$ and 100 cm (rows) and at incidence angles: $\theta = 0°$, 30° and 45° (columns).

45°. It is noteworthy that the specular component is similar in magnitude and location to the rectangular sample cases (see the first row of Fig. 3). On the other hand, the side-lobe components seem to be less localized in k-space for the circular samples. Note the ring outside of the radiation circle in Fig. 4(a). At this point, the hypothesis is that in the case of circular samples, a Bessel function would replace the sinc functions in Eq. (2) (valid for rectangular samples) - a formal derivation is to be done. Interestingly, the shape of the sample influences the wave-number spectrum, which indicates the potential of the technique to investigate the edge diffraction phenomenon more deeply in the future.

5.2 Absorption and surface impedance

Once the wave-number spectrum is computed, its information can be used to reconstruct the surface impedance with Eq. (8). We follow the approach in Refs. [12, 14, 18] and reconstruct the surface impedance at a small patch area of 10×10 cm^2 centered at the surface of the sample. The area contains 21×21 point-wise impedances and the spatial average is computed and taken as the sample's surface impedance, from which the absorption coefficient is calculated with Eq. (9).

Fig. 5 displays the absorption coefficient as a function of the sample shape and size for the 25 mm and the 100 mm thick samples at $\theta = 0°$. The cur-

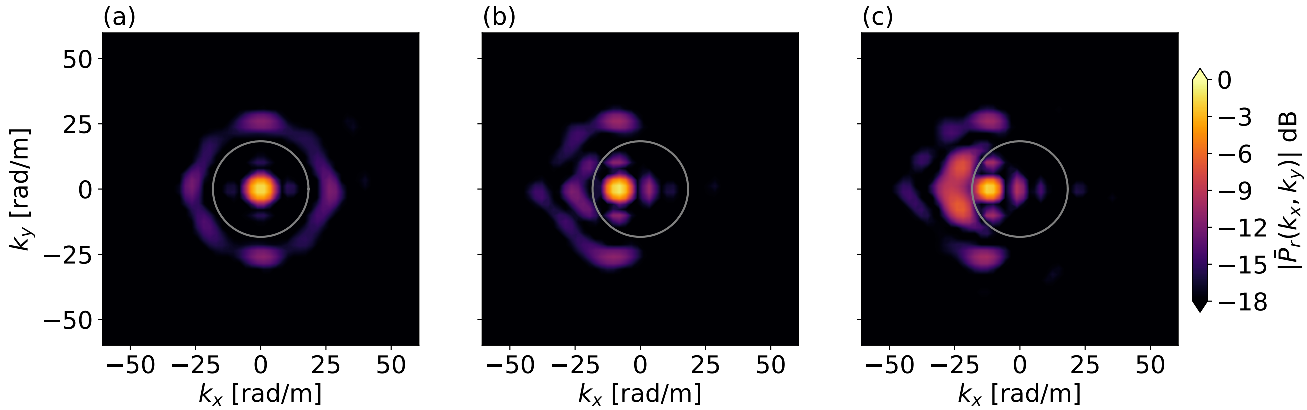

Figura 4: Reflected wave-number spectra at 1000 Hz for circular samples of radius: $a = 20$ cm at incidence angles: $\theta = 0°$, $30°$ and $45°$.

ves labeled as "True" correspond to the ground truth, i.e. the boundary condition prescribed to the BEM mesh. The remaining curves follow from the deduction algorithm using numerical experiments with the BEM. The ones labeled as "sq: $L = (\cdot)$ cm" are obtained from sound fields above squared samples with varying sizes. The one labeled as "circ: $a = 20$ cm" follow from the sound field above the circular sample.

It is noteworthy that the estimated absorption coefficient hardly changes with the sample size and shape, and it is very close to the True absorption coefficient above 400 Hz. Thus, the estimated surface impedance of the finite absorbers depends just slightly on the sample size and shape and is an accurate representation of an infinite absorber. This is attributed to the inclusion of the evanescent waves in the sound field model, which is a precise representation in the near field of the sample. In contrast, one can think that a single receiver is subjected to all the main and side lobes of the actual k-space. Thus, to estimate the surface impedance from single-point measurements, choosing the sensor's position might be critical since the sound field can contain high spatial frequency components. On the other hand, the spatial measurement of the sound field and the reconstruction of the surface impedance seem to represent the phenomenon well. Furthermore, we note that for less absorbing samples, the actual value of the particle velocity tends to be small in the low-frequency range, as the samples are reflective. In such cases, deviations arise when trying to reconstruct the particle velocity from pressure data [28], leading to the larger deviations for Fig. 5a.

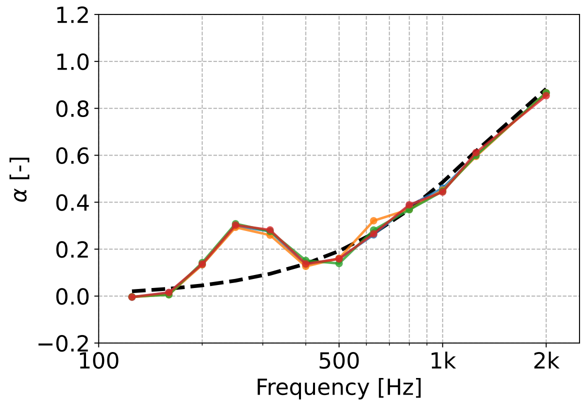

(a) $d = 25$ mm

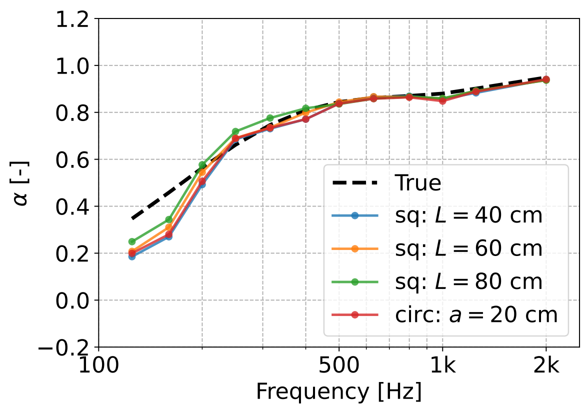

(b) $d = 100$ mm

Figura 5: Absorption coefficient of samples with different sizes at incidence angles of $0°$ and thickness $d = 25$ mm and $d = 100$ mm.

6. CONCLUSIONS

This study investigated the diffraction effects on the *in situ* measurement of finite porous absorbers with spatial analysis and the resulting wave-number spectrum. The theoretical wave-number spectrum agrees with the regularized solution from array data. The wave-number spectrum is a practical approach to analyzing the main components related to edge diffraction and can capture features related to the size and shape of the sample. The *k*-space displays the main propagating components associated with the incident and specularly reflected sound field. It contains significant side-lobe components associated with the sound source localization relative to the edges of the samples. The strength of such side-lobe components tends to diminish as the sample size and spatial frequency increase. Some of the significant side-lobe components are evanescent plane waves traveling in directions parallel to the sample's surface. For the circular sample, the side-lobe components tend to be less localized in the *k*-space domain than for the rectangular ones. The surface impedance was reconstructed at a small patch area at the center of the absorber. Estimating the absorption coefficient is difficult for low absorbent samples due to the innate imprecisions in reconstructing the particle velocity from pressure data. The use of both propagating and evanescent waves in the sound field model led to an estimation of the absorption coefficient just slightly influenced by the size and shape of the sample.

7. AGRADECIMENTOS

The authors would like to thank the National Research Council of Brazil (CNPq - *Conselho Nacional de Desenvolvimento Científico e Tecnológico*) for the partial financial support to this research paper (*Projeto Universal*: n° 402633/2021-0).

REFERENCES

[1] ISO 10534-2: Acoustics - Determination of sound absorption coefficient and impedance in impedance tubes-Part 2: Transfer-function method. Technical report, International Organization for Standardization, 2001.

[2] ISO 354: Measurement of sound absorption in a reverberation room. Technical report, International Organization for Standardization, 2003.

[3] Thomasson, S. I. On the absorption coefficient. *Acustica*, 44:265–273, 1980.

[4] Bruijn, A. A mathematical analysis concerning the edge effect of sound absorbing materials. *Acustica*, 28:33–44, 1973.

[5] Pereira, M; Mareze, PH; Godinho, L; Amado-Mendes, P e Ramis, J. Proposal of numerical models to predict the diffuse field sound absorption of finite sized porous materials–bem and fem approaches. *Applied Acoustics*, 180:1–13, 2021.

[6] Brandão, E.; Lenzi, A. e Paul, S. A review of the in situ impedance and sound absorption measurement techniques. *Acta Acustica united with Acustica*, 101: 443 – 463, 2015.

[7] Kimura, K. e Yamamoto, K. The required sample size in measuring oblique incidence absorption coefficient experimental study. *Applied Acoustics*, 63:567–578, 2002.

[8] Hirosawa, K.; Takashima, K.; Nakagawa, H.; Kon, M.; Yamamoto, A. e Lauriks, W. Comparison of three measurement techniques for the normal absorption coefficient of sound absorbing materials in the free field. *The Journal of the Acoustical Society of America*, 126 (6):3020–3027, 2009.

[9] Brandão, E.; Lenzi, A. e Cordioli, J. Estimation and minimization of errors caused by sample size effect in the measurement of the normal absorption coefficient of a locally reactive surface. *Applied Acoustics*, 73: 543 – 556, 2012.

[10] Tamura, M. Spatial Fourier transform method of measuring reflection coefficients at oblique incidence. I: Theory and numerical examples. *The Journal of the Acoustical Society of America*, 88(5):2259 – 2264, 1990.

[11] Tamura, M.; Allard, J.F. e Lafarge, D. Spatial Fourier-transform method for measuring reflection coefficients at oblique incidence. II: Experimental results. *The Journal of the Acoustical Society of America*, 97 (4):2255 – 2262, 1995.

[12] Richard, A. e Fernandez-Grande, E. Comparison of two microphone array geometries for surface impedance estimation. *The Journal of the Acoustical Society of America*, 146(1):501 – 504, 2019.

[13] Nolan, M. Estimation of angle-dependent absorption coefficients from spatially distributed in situ measurements. *The Journal of the Acoustical Society of America*, 147(2):EL119–EL124, 2020.

[14] Richard, A.; Fernandez-Grande, E.; Brunskog, J. e Jeong, C-H. Estimation of surface impedance at oblique incidence based on sparse array processing. *The Journal of the Acoustical Society of America*, 141 (6):4115 – 4125, 2017.

[15] Hald, J.; Song, W.; Haddad, K.; Jeong, C-H e Richard, A. In-situ impedance and absorption coefficient measurements using a double-layer microphone array. *Applied Acoustics*, 143:74 – 83, 2019.

[16] Ottink, M.; Brunskog, J.; Jeong, C-H; Fernandez-Grande, E.; Trojgaard, P. e Tiana-Roig, E. In situ measurements of the oblique incidence sound absorption coefficient for finite sized absorbers. *The Journal of the Acoustical Society of America*, 139(1):41 – 52, 2016.

[17] Richard, A.; Fernández Comesaña, D.; Brunskog, J.; Jeong, C-H e Fernandez-Grande, E. Characterization of sound scattering using near-field pressure and particle velocity measurements. *The Journal of the Acoustical Society of America*, 146(4):2404 – 2414, 2019.

[18] Brandão, Eric e Fernandez-Grande, Efren. Analysis of the sound field above finite absorbers in the wave-number domain. *The Journal of the Acoustical Society of America*, 151(5):3019–3030, 2022.

[19] Brunskog, Jonas. The forced sound transmission of finite single leaf walls using a variational technique. *The Journal of the Acoustical Society of America*, 132 (3):1482–1493, 2012.

[20] Maynard, Julian D; Williams, Earl G e Lee, Y. Nearfield acoustic holography: I. Theory of generalized holography and the development of NAH. *The Journal of the Acoustical Society of America*, 78(4): 1395–1413, 1985.

[21] Hald, J. Basic theory and properties of statistically optimized near-field acoustical holography. *The Journal of the Acoustical Society of America*, 125(4):2105–2120, 2009.

[22] Jacobsen, Finn e Jaud, Virginie. Statistically optimized near field acoustic holography using an array of pressure-velocity probes. *The Journal of the Acoustical Society of America*, 121(3):1550–1558, 2007.

[23] Nolan, Mélanie; Verburg, Samuel A; Brunskog, Jonas e Fernandez-Grande, Efren. Experimental characterization of the sound field in a reverberation room. *The Journal of the Acoustical Society of America*, 145(4): 2237–2246, 2019.

[24] Hansen, Per Christian. *Discrete inverse problems: insight and algorithms*. 3600 Market Street, 6th Floor, Philadelphia, PA 19104-2688 USA: Siam, 2010. volume 7. Sec. 5.3.

[25] Miki, Yasushi. Acoustical properties of porous materials-Modifications of Delany-Bazley models. *Journal of the Acoustical Society of Japan (E)*, 11 (1):19–24, 1990.

[26] Allard, J.F. e Atalla, N. *Propagation of sound in porous media: modeling sound absorbing materials*. West Sussex, PO19 8SQ, United Kingdom: Wiley, 2009. Cap. 11.

[27] Williams, Earl G e Maynard, Julian D. Numerical evaluation of the rayleigh integral for planar radiators using the fft. *The Journal of the Acoustical Society of America*, 72(6):2020–2030, 1982.

[28] Jacobsen, Finn e Liu, Yang. Near field acoustic holography with particle velocity transducers. *The Journal of the Acoustical Society of America*, 118(5):3139–3144, 2005.